Petroleum Science 18 (2021) 1867–1876

Contents lists available at ScienceDirect

Petroleum Science

journal homepage: www.keaipublishing.com/en/journals/petroleum-science

Original Paper

Mo supported on natural rectorite catalyst for slurry-phase hydrocracking of vacuum residue: An effect of calcination

Qing-Yan Cui*, Hao-Bin Zhang, Ting-Hai Wang, Chao Yan, Yan-Ning Cao, Yuan-Yuan Yue, Li-Long Jiang, Xiao-Jun Bao

College of Chemical Engineering, Fuzhou University, Fuzhou, 350108, China

ARTICLE INFO

Article history:
Received 21 December 2020
Accepted 29 March 2021
Available online 11 September 2021

Edited by Xiu-Qiu Peng

Keywords:
Natural rectorite
Catalyst
Slurry-phase hydrocracking
Vacuum residue
Calcination

ABSTRACT

In order to develop high-efficiency and low-cost catalyst for the slurry-phase hydrocracking of vacuum residue (VR), the catalyst supported on natural rectorite was prepared, and the effect of calcination modification of rectorite on the catalyst properties and performance was investigated. The support of rectorite and catalyst were characterized by XRD, FTIR, Py-FTIR, H_2-TPR and XPS to examine their structures and properties. The comparative reaction results show that VR conversions for the catalysts supported on calcined rectorite were similar with that on raw rectorite, possibly due to the VR cracking reaction controlled by the thermal cracking following free radical mechanism because of few acid sites observed on the catalysts surface. However, the yields of naphtha and middle distillates for the various catalysts were obviously different, and increased following as Rec-Mo (40.4 wt%) < Rec-600-Mo (52.7 wt %) < Rec-450-Mo (53.5 wt%) < Rec-500-Mo (61.7 wt%), indicating that the calcination of rectorite favored the enhancement of the yields of naphtha and middle distillates for the catalyst in the slurry-phase hydrocracking process, it is attributed that the higher sulfidation degree of molybdenum oxide species on the catalyst surface promoted hydrogenation reaction, thus restrained over-cracking reaction of intermediate product to produce gas.

1. Introduction

The continuously growing demand for clean transportation fuels with the depletion of conventional petroleum reserves promotes an increase of poor and heavy oil upgrading. Therefore, it is significant to efficiently convert the residual oil into light fractions oil in the refining industry, in which the composition of residual oil is complex, containing paraffinic, naphthenic and aromatic hydrocarbons with high contents of sulfur (S), nitrogen (N), vanadium (V), nickel (Ni) and so on, but it is difficult and challenging to achieve the efficient conversion of residual oil. Among several residual oil conversion processes, slurry-phase hydrocracking of heavy oil technology is an alternative technology, which has been attracting great attention because of its ability to process various heavy oils and achieve a higher feedstocks conversion (Go et al., 2018; Lim et al., 2018). It is known that the catalyst plays a significant role on the performance in the slurry-phase hydrocracking process.

Slurry-phase hydrocracking catalysts mainly include oil-soluble dispersed catalysts and solid powder dispersed catalysts (Watanabe et al., 2002; Al-Attas et al., 2019). Oil-soluble dispersed catalysts were obtained by introducing transitional metals (such as Mo, Ni, Co and Fe) into oil soluble precursors to form organometallic compounds (Kang et al., 2020; Yang et al., 2019; Li et al., 2019). The active metal of catalyst can rapidly saturate the free radicals produced via β-scission reaction of C—C by incorporating hydrogen into the cracked active hydrocarbons, which favor to limit the aromatic condensation reaction and over cracking reaction (Bellussi et al., 2013; Nguyen et al., 2016; Kim et al., 2017). It has been found that oil-soluble Mo catalyst exhibited higher performance compared with other metals catalysts in the slurry-phase hydrocracking process (Kim et al., 2018; Liu et al., 2019). Moreover, the synergy effect of bimetals catalyst on the heavy oil conversion and the yield of light distillates oil was observed (Kim et al., 2019; Nguyen et al., 2015). Oil-solution catalysts possess great catalytic performance in the slurry-phase hydrocracking, but the high-cost

* Corresponding author.
E-mail address: qycui@fzu.edu.cn (Q.-Y. Cui).

https://doi.org/10.1016/j.petsci.2021.09.019

during organometallic compounds preparation restrict their wide application in the petroleum refining industry.

Solid powder dispersed catalysts, generally inorganic minerals, were widely employed in the early stage of the development of slurry-phase hydrocracking technology, in which inorganic minerals were considered as the hydrogenation active phase and coke carries in the slurry-phase hydrocracking process (Sanaie et al., 2001; Matsumura et al., 2005). Matsumura et al., (2005) used the natural limonite as catalyst to upgrade Brazilian Marlim vacuum residue (VR), VR conversion was less than 80 wt%, C5-340 °C fraction yield was about 34 wt%, and the coke yield was higher than 5 wt%. Red mud containing a mixture of Fe, Al and Ti oxide was employed for the slurry-phase hydrocracking of VR, the result showed that VR conversion was about 65 wt%, and the yield of naphtha and diesel was lower than 34 wt%, as well as the active phase for the hydrocracking reaction was pyrrhotite ($Fe_{(x-1)}S_x$) derived from iron oxide (Nguyen-Huy et al. 2012, 2013). Quitian et al. (Quitian et al., 2016) found that ore catalyst of molybdenite and hematite were able to inhibit the gas and coke formation caused by decomposition and condensation reactions, and promote the hydrogenation of the free radicals formed primarily via the thermal cracking of C–C bond. Although the inorganic minerals as catalyst have an advantage over the low cost in the slurry-phase hydrocracking process, their inferior catalytic activity can't meet the demand for highly efficient conversion of heavy oils.

In order to overcome the drawbacks of oil-solution dispersed catalysts and fine inorganic minerals catalysts, the transitional metals such as Mo, Co and Ni were supported on carbon, alumina, silica-alumina, even inorganic minerals to prepare the hydrocracking catalysts, which not only can provide more hydrogenation active sites, but also play a role of coke carries (Looi et al., 2012; Park et al., 2019; Viet et al., 2012). MoS_2-amorphous-silica-alumina (ASA) catalyst employed in the slurry-phase hydrocracking promoted the cracking reaction and changed favorably the product distribution (Sanchez et al., 2018). Puron et al., (2013) found that $NiMo/Al_2O_3$ catalyst exhibited higher asphaltenes conversion with lower coke deposition and a reduced gas yield at achieving similar VR conversion compared with NiMo/ASA catalyst in the slurry-phase hydrocracking of Maya VR, due to its larger pore lessening diffusion limitation of asphaltenes molecules. Sahu et al., (2016) reported that Ni–Mo supported on goethite catalyst showed VR conversion of 80 wt% with the low boiling point liquid products of about 70 wt%, and found the products distribution depending on the physical and chemical properties of the catalysts. In comparison with the chemical synthesis materials of ASA and Al_2O_3, the natural minerals not only have an advantage in very low cost, but also contains some metals such as Ti and Zn, especially Fe, which can transform to sulfided iron ($Fe_{1-x}S$) acted as the hydrocracking active sites (Du et al., 2018). Cortes et al., (2019) employed the modified vermiculite as support to prepare the hydrocracking catalyst for Athabasca Bitumen, and observed that Fe in vermiculite favored to improve the catalyst activity for the Bitumen conversion. Our group has studied the catalyst supported on natural bauxite modified by acid-treatment and hydrothermal method for hydrocracking of coal tar, the results shows that the acid-treatment and hydrothermal modifications can enhance the catalyst performance in the hydrocracking process (Yue et al. 2016, 2018). However, the catalyst presented lower conversion even though using relatively light oil of coal tar with boiling point higher than 510 °C fraction less than 40 wt% as feedstock, while the processes of acid-treatment and hydrothermal modification led to wastewater discharge and increasing energy consumption.

In this study, natural rectorite after calcination was used as support to prepare Mo catalysts for the slurry-phase hydrocracking of VR, in which the effect of calcination modification on the natural rectorite properties and catalyst performance was investigated. The supports of calcined rectorite and catalysts were characterized by XRD, FTIR, Py-FTIR, H_2-TPR and XPS, as well as the catalyst performance was evaluated in an autoclave reactor with VR as feedstock to principally examine VR conversion and the yield of naphtha and middle distillates in the hydrocracking process. This work is significant for the development of high-efficiency and low-cost catalysts for the slurry-phase hydrocracking.

2. Experimental section

2.1. Feedstock

Vacuum residue (VR) used as feedstock for the slurry-phase hydrocracking was supplied by China Petrochemical Corporation, its properties are shown in Table 1.

2.2. Catalysts

Natural rectorite was supplied by Zhongxiang Rectorite Co., Ltd. (Hubei Province, P. R. China), its chemical analysis compositions are shown in Table 2. The calcination modification of natural rectorite was conducted at 450, 500 and 600 °C, which are denoted as Rec-450, Rec-500 and Rec-600. Mo supported on calcined rectorite catalyst was prepared by using the incipient wetness impregnation method with aqueous solution of ammonium molybdate tetrahydrate ($(NH_4)_6Mo_7O_{24}\cdot 4H_2O$, Adamas, 98%). The wet catalyst after set at 25 °C for 12 h was dried at 120 °C for 10 h, and then calcined at 500 °C for 4 h. The content of MoO_3 in catalyst is 5 wt%. The catalysts are designated as Rec-Mo, Rec-450-Mo, Rec-500-Mo and Rec-600-Mo.

2.3. Characterizations

X-ray diffraction (XRD) analysis of the sample was performed on an Ultima IV diffractometer with Co Kα radiation at 40 kV and 40 mA, and the pattern was recorded in the 2θ range from 5 to 90° with a step of 0.02°. Fourier transform infrared (FTIR) was employed to examine the framework structure of natural rectorite, which was carried out on a Nicolet iS 10 spectrometer with the sample diluted by KBr at the ratio of 1:100, and the FTIR spectra were recorded in the wavenumber range from 4000 to 400 cm^{-1} with scans of 32. Pyridine adsorbed FTIR (Py-FTIR) of sample was conducted after heated at 350 °C for 5 h under a vacuum of 1.3×10^{-3} Pa, and the adsorption of pure pyridine vapor at 30 °C for 20 min was followed. Adsorbed pyridine was removed by evacuating at 200 and 350 °C. H_2 temperature programmed reduction (H_2-TPR) of natural rectorite and catalyst was carried out on an ASAP-2920 instrument with a thermal conductivity detector (TCD).

Table 1
Compositions and properties of VR.

Properties	VR
Density, kg m^{-3} 20 °C	985.5
Viscosity, 100 °C	84.7
Ni, ppm	46.2
V, ppm	111
S, wt%	3.1
N, ppm	3427
Conradson carbon residue, wt%	10.7
Boiling point, °C	
<180	0.0
180–350	2.1
350–520	31.4
>520	66.5

Table 2
Chemical analysis compositions of natural rectorite.

Components, wt%	SiO_2	Al_2O_3	Fe_2O_3	CaO	SO_3	TiO_2	K_2O	NaO
Rectorite	38.6	31.3	8.2	7.4	7.1	4.0	1.4	0.7

The sample was pretreated at 300 °C for 30 min under Ar atmosphere, and then heated from 50 to 950 °C with a rate of 10 °C/min in the 10 vol% H_2/Ar stream. X-ray photoelectron spectroscopy (XPS) analysis of catalyst was performed on a Thermo Scientific ESCALAB 250Xi instrument with a monochromatic Al Kα source, and C1s peak with a binding energy of 284.6 eV and Al 2p peak with a binding energy of 74.6 eV were used as the references to calibrate the binding energy scale of Mo species. XPS spectra were recorded by using a XPSPEAK41 software after a background subtraction, and Gaussian-Lorentzian function was used for the spectrum deconvolution. The relative concentrations of the species of MoS_2, MoS_xO_y and Mo^{6+} oxide for each sulfided catalyst were determined through their corresponding peak area. For example, the relative MoS_2 concentration was calculated as following:

$$[MoS_2](\%) = A_{MoS2}/(A_{MoS2}+A_{MoSxOy} + A^{6+}_{Mo})$$

where A_X represents the peak area of species X.

2.4. Catalyst evaluation

The slurry-phase hydrocracking performances of catalysts were evaluated in a 300 mL stainless-steel autoclave reactor using VR as a feedstock. VR, catalyst and appropriate sulfur powder were loaded into the reactor with the catalyst content of 5 wt%. Prior to the hydrocracking reaction, the catalyst was presulfurized with sulfur powder at 250 °C for 35 min and 350 °C for 35 min. The hydrocracking of VR was carried out at 420 °C under an initial H_2 pressure of 13 MPa with the H_2 to oil ratio (v/v) of 1000 for 90 min with vigorous agitation. After the hydrocracking reaction, the autoclave reactor was rapidly cooled to ambient temperature. The mixture of product and catalyst was collected, and then centrifuged to separate the liquid product and solid residue. The solid residue was washed with toluene to obtain the toluene insoluble, which included catalyst and coke. The liquid product was divided into four fractions on the basis of the boiling point (BP) in a decompression distillation plant, which are naphtha (BP < 180 °C), middle distillates (BP 180–350 °C), vacuum gas oil (VGO, BP 350–520 °C) and VR (BP > 520 °C). VR conversion and the yields of gas, naphtha, middle distillates, VGO and coke were calculated as following:

VR conversion (%) = (mass of >520 °C fraction in feed > mass of >520 °C fraction in product) / (mass of >520 °C fraction in feed) × 100%

Gas yield (wt%) = (mass of gas in product) / (mass of the feed) × 100%

Naphtha yield (wt%) = (mass of <180 °C fraction in product / mass of the feed) × 100%

Middle distillates yield (wt%) = (mass of 180–350 °C fraction in product −mass of 180–350 °C fraction in feed) / (mass of the feed) × 100%

VGO yield (wt%) = (mass of 350–520 °C fraction in product − mass of 350–520 °C fraction in feed) / (mass of the feed) × 100%

Coke yield (wt%) = (mass of coke) / (mass of the feed) × 100%

3. Results and discussion

3.1. Structure and properties of rectorite

3.1.1. Crystalline structure

Fig. 1 shows the XRD patterns of raw rectorite and rectorites calcined at different temperatures. The peaks at about $2\theta = 7.0^o$ and 19.8^o were assigned to the characteristic diffraction peaks of rectorite crystalline structure (Zhang et al., 2010; Bao et al., 2019), while there were some impurities such as rutile TiO_2 corresponding to $2\theta = 27.4^o$ and hematite Fe_2O_3 corresponding to $2\theta = 33^o$ and 35.5^o in the raw nature rectorite (Nguyen-Huy et al., 2012; Liu et al., 2019), because the rectorite contained Fe_2O_3 of 8.2 wt% and TiO_2 of 4.0 wt% on the basis of the chemical compositions analysis in Table 2. The intensity of diffraction peaks of rectorite crystalline structure decreased after calcination, especially the peak at $2\theta = 7.0^o$, indicating that the crystalline structure of rectorite was destroyed during the calcination process, possibly due to the loss of interlay water under the high temperature calcining. No obvious change was observed for the diffraction peaks of nature rectorites calcined at different temperatures, indicating the calcination temperature higher than 450 °C had no remarkable effect on the rectorite crystalline structure.

FT-IR spectra of nature rectorites calcined at different temperature are shown in Fig. 2. The peaks at 3640 and 3430 cm^{-1} observed in IR spectra of rectorites were assigned to the bending vibration of hydrogen band of the hydroxyl stretching in SiOH and interlaminar water, respectively. The peak at 1040 cm^{-1} was associated with the in-plane Si–O–Si stretching vibration, and the peak at 705 cm^{-1} was ascribed to the bending vibration of Si–O–Al (Zheng et al., 2013). The peak at 3640 cm^{-1} corresponding to the hydrogen band vibration of SiOH hydroxyl stretching disappeared after rectorite calcination because of the −OH dropping from SiOH structure. Moreover, the intensity of peak at 3430 cm^{-1} dramatically decreased for the rectorite calcined at 600 °C, nearly disappeared, indicating that the interlaminar water fell off from the rectorite structure when heated at 600 °C. In addition, all IR peaks positions of rectories had no shift during the calcination process.

3.1.2. Acid properties

The acid properties of the calcined rectorites were investigated by Py-FTIR. The Py-FTIR spectra of the calcined rectorites measured at 200 and 350 °C are shown in Fig. 3. The band at 1450 and 1540 cm^{-1} are assigned to the Lewis (L) and Brønsted (B) acid sites, respectively (Tan et al., 2008; Wei et al., 2019). No obvious peak was observed for raw rectorite at both of 200 and 350 °C in the Py-FTIR spectra. While there was slightly weak peak at 1450 cm^{-1} for the calcined rectorite measured at 200 °C. The detail amounts of acid sites at 200 and 350 °C for the calcined rectorites are summarized in Table 3. It is found that the amount of acid sites of calcined rectorites had no distinct increase compared with that of raw rectorite, which were less than 10 μmol/g for both L and B acid sites, suggesting that the calcined modification did nearly not increase acid sites on the rectorite.

3.1.3. H_2-TPR results

Fig. 4 displays H_2-TPR profiles of nature rectorites calcined at various temperatures. The reduction peaks of H_2-TPR profiles can reflect the hydrogen consumption. Raw rectorite exhibited two reduction peaks, which were at center of 495 and 770 °C, respectively. Nature rectorite contained Fe_2O_3 with the content of 8.2 wt% more than other metallic oxides, except for Al_2O_3 and SiO_2, according to the chemical compositions analysis of rectorite. Thus, the

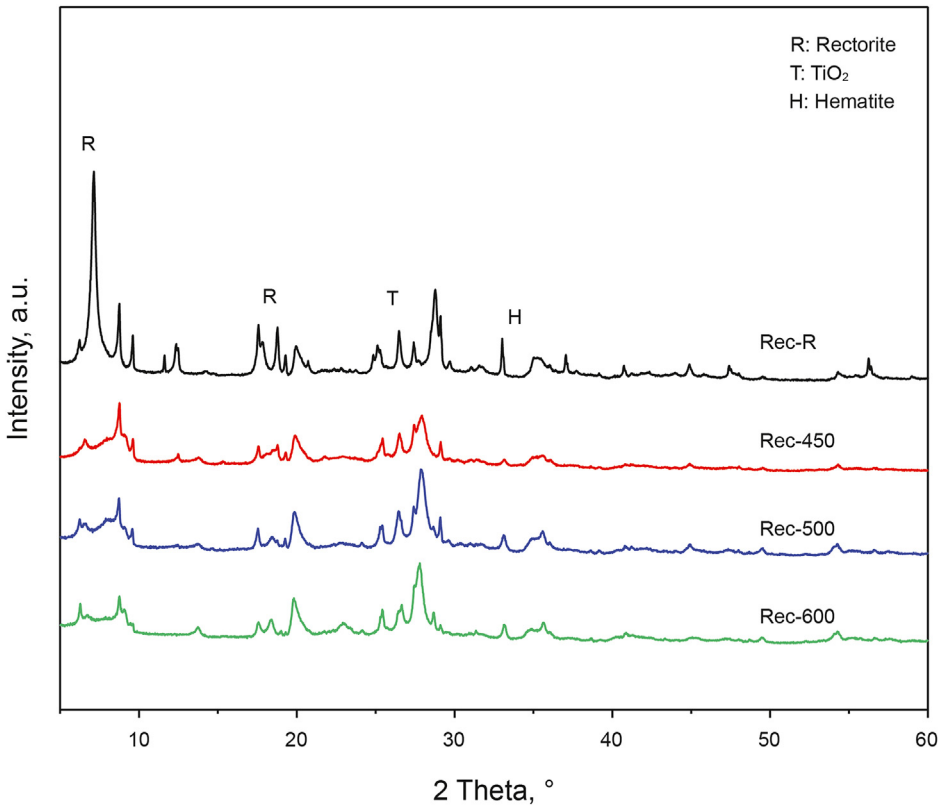

Fig. 1. XRD patterns of rectorites calcined at different temperatures.

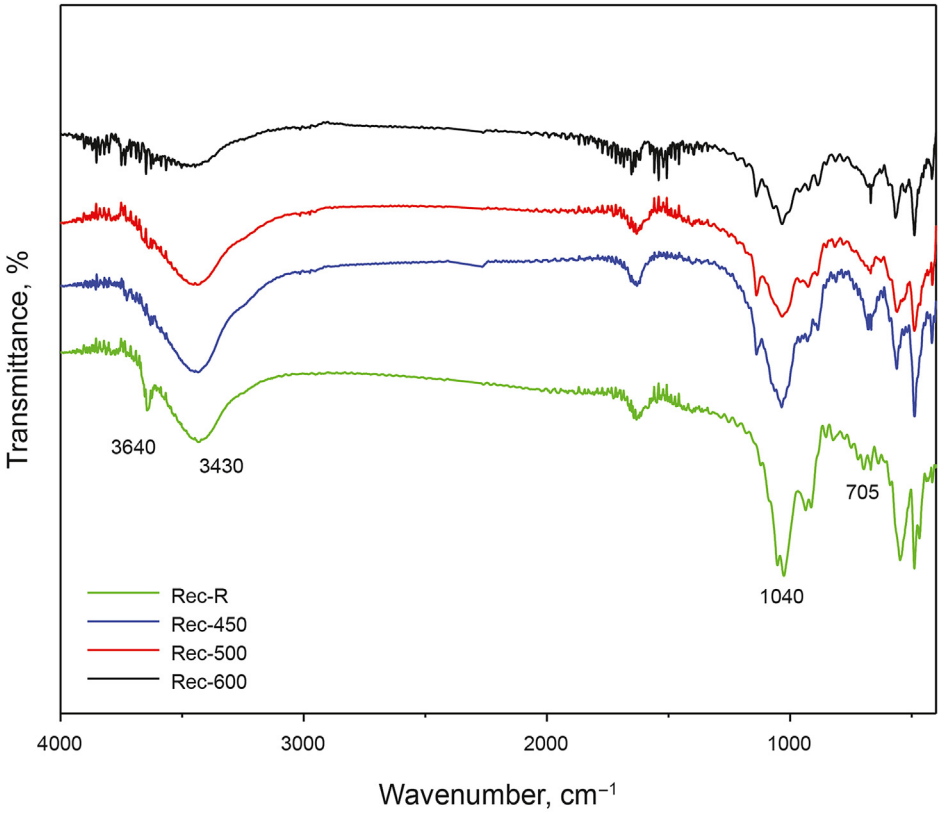

Fig. 2. FT-IR spectra of rectorites calcined at different temperatures.

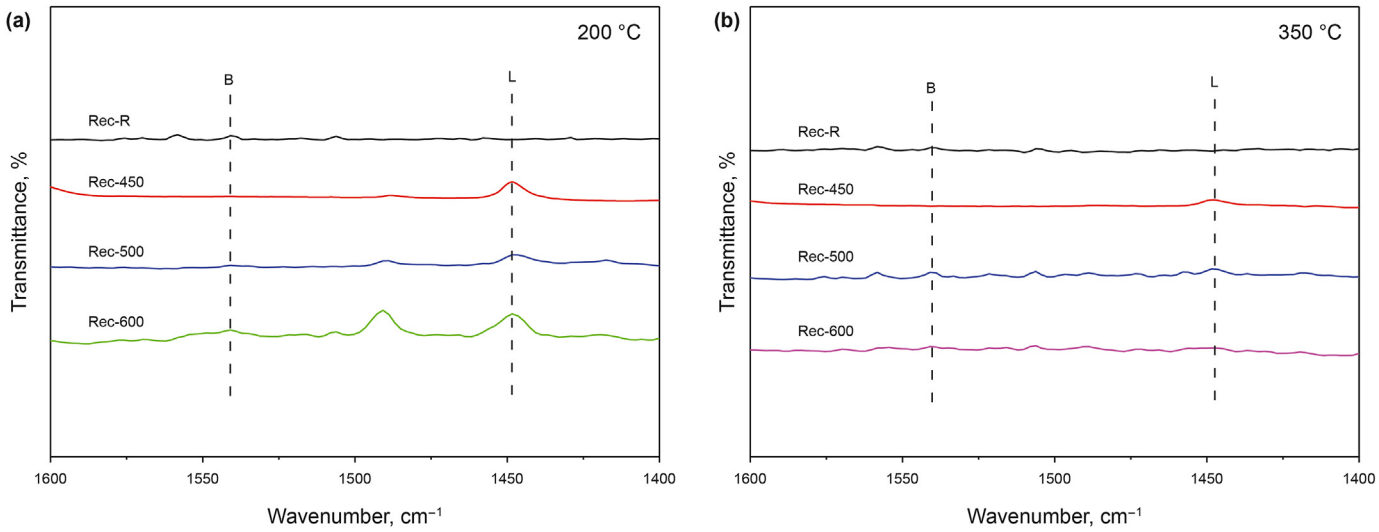

Fig. 3. Py-FTIR spectra of calcined rectorites measured at (a) 200 °C and (b) 350 °C.

Table 3
The amount of acid sites of calcined rectorites.

Samples	Temperature,°C	L, μmol/g	B, μmol/g	L + B, μmol/g
Rec-raw	200	0.3	0.7	1.0
	350	0.2	0.5	0.7
Rec-450	200	7.6	0.1	7.7
	350	2.7	0.0	2.7
Rec-500	200	2.3	1.0	3.3
	350	0.9	0.9	1.8
Rec-600	200	4.2	1.1	5.3
	350	1.8	0.9	2.7

peaks of rectorite were considered as the reduction peaks of iron oxides species. The reduction steps of iron oxides species in hydrogen usually follows as: from Fe_2O_3 to Fe_3O_4, and then from Fe_3O_4 to FeO, finally from FeO to Fe, as reported in the literatures (Mogorosi et al., 2012; Cheng et al., 2015). Hence, the peak at center of 495 °C was ascribed to the reduction of hematite (Fe_2O_3) to magnetite (Fe_3O_4), and the peak at center of 770 °C was attributed to formation of Fe though the reduction of FeO. The rectorite calcined at 450 °C also showed two reduction peaks, and the reduction peak positions were similar with that of raw rectorite, suggesting no new iron oxides species formation, but the area of peak at 495 °C was remarkably larger than that of raw rectorite, it may be that calcination made inert iron oxides into active iron phase. A peak at center of 615 °C appeared for the rectorite calcined at 500 °C, associating with the reduction of magnetite to FeO, and it became stronger accompanied with the peak at 490 °C becoming weaker for the rectorite calcined at 600 °C, indicating that some amount of hematite converted into magnetite in the rectorite when calcined at the temperature higher than 500 °C.

3.2. Catalysts properties

3.2.1. H_2-TPR analysis of catalysts

H_2-TPR profiles of Mo catalysts supported on rectorites calcined at different temperatures are shown in Fig. 5. It is clear that there were two reduction peaks centered at the temperature of 560 and 780 °C for all Mo catalysts supported on rectorites, in which the peak at 560 °C was ascribed to the reduction of octahedral Mo^{6+} species to tetrahedral Mo^{4+} species, Fe_2O_3 species to Fe_3O_4 species and Fe_3O_4 species to FeO species, as well as the peak at 780 °C was attributed to the tetrahedral Mo^{4+} species to Mo and FeO species to metallic iron. In comparison with the catalyst supported on raw rectorite, the two reduction peaks positions had no obvious shift for the catalyst supported on calcined rectorites, however, remarkable change of peak area was observed for the catalyst supported on calcined rectorites, especially the low-temperature reduction peak. The low-temperature reduction peak area of catalysts supported on calcined rectorites decreased compared with that of catalyst supported on raw rectorite, and it changed in the order of Rec-Mo > Rec-500-Mo > Rec-450-Mo ≈ Rec-600-Mo, indicating the amount of octahedral Mo^{6+}, Fe_2O_3 and Fe_3O_4 species on catalyst of rectorite calcined at 500 °C was slightly less than that on catalyst of raw rectorite, but more than those on catalyst of rectorite calcined at 450 and 600 °C, it may be that the change of hydroxyl on rectorite during the calcination had an effect on the Mo species phase formation on the catalysts surface.

3.2.2. XPS analysis

The chemical surface compositions of sulfided catalysts supported on rectorites were investigated by XPS. Fig. 6 displays Mo 3d XPS spectra and deconvolution results of sulfided catalysts supported on rectorites calcined at various temperatures. The Mo 3d XPS spectra include three doublets, the doublets with bending energy at 229.3 and 232.5 eV are related to Mo $3d_{5/2}$ and Mo $3d_{3/2}$ levels for the Mo^{4+} in MoS_2 phase species, the doublets with bending energy at 230.5 and 233.8 eV are ascribed to Mo $3d_{5/2}$ and Mo $3d_{3/2}$ levels for the Mo^{5+} in MoS_xO_y oxysulfide species, and the doublets with bending energy at 232.7 and 235.9 eV are assigned to Mo $3d_{5/2}$ and Mo $3d_{3/2}$ levels for the Mo^{6+} in MoO_3 oxide species (Nikulshin et al., 2014; Pimerzin et al., 2017; Zhou et al., 2018). The deconvolution results of different catalysts based on XPS spectra are summarized in Table 4. It is found that the sulfidation degree of Mo species (Mo^{4+} proportion) on the calcined rectorites catalysts was higher than that on raw rectorite catalyst, especially the catalyst on rectorite calcined at 500 °C, it may be ascribed that calcination modulated the surface hydroxyl on rectorite, further influenced the interaction of Mo species and rectorite. In general, the catalyst with high sulfidation degree presents high hydrogenation activity in the hydrocracking and/or hydrotreating process (Nikulshin et al., 2014; Pimerzin et al., 2017; Cui et al., 2013; Liu et al., 2020).

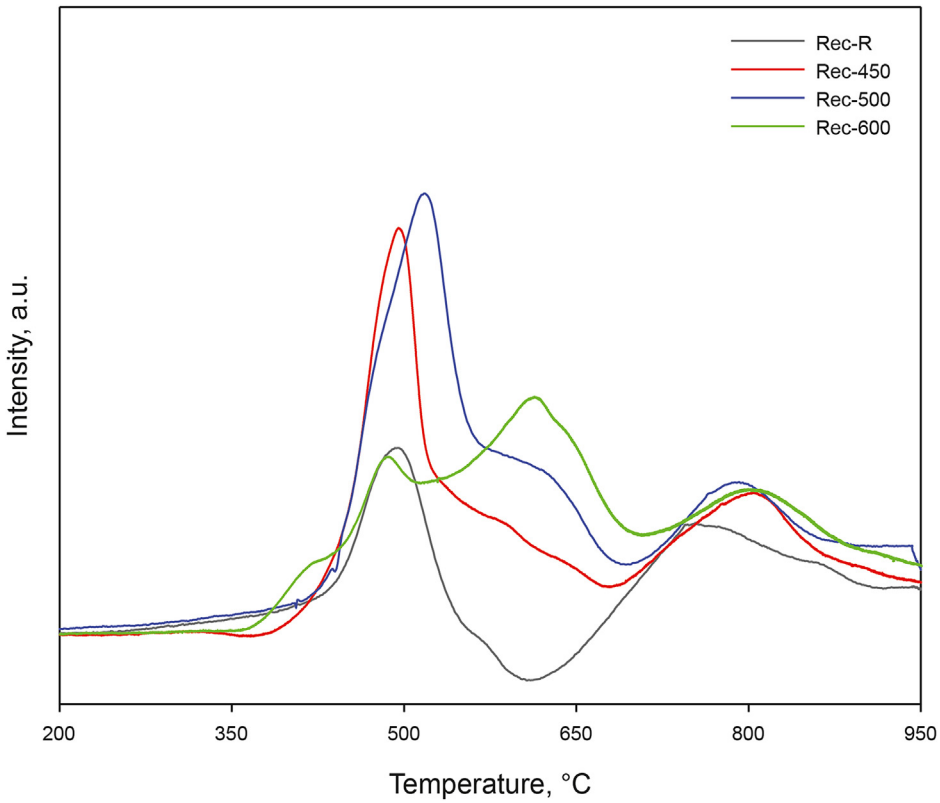

Fig. 4. H_2-TPR profiles of nature rectorites calcined at different temperatures.

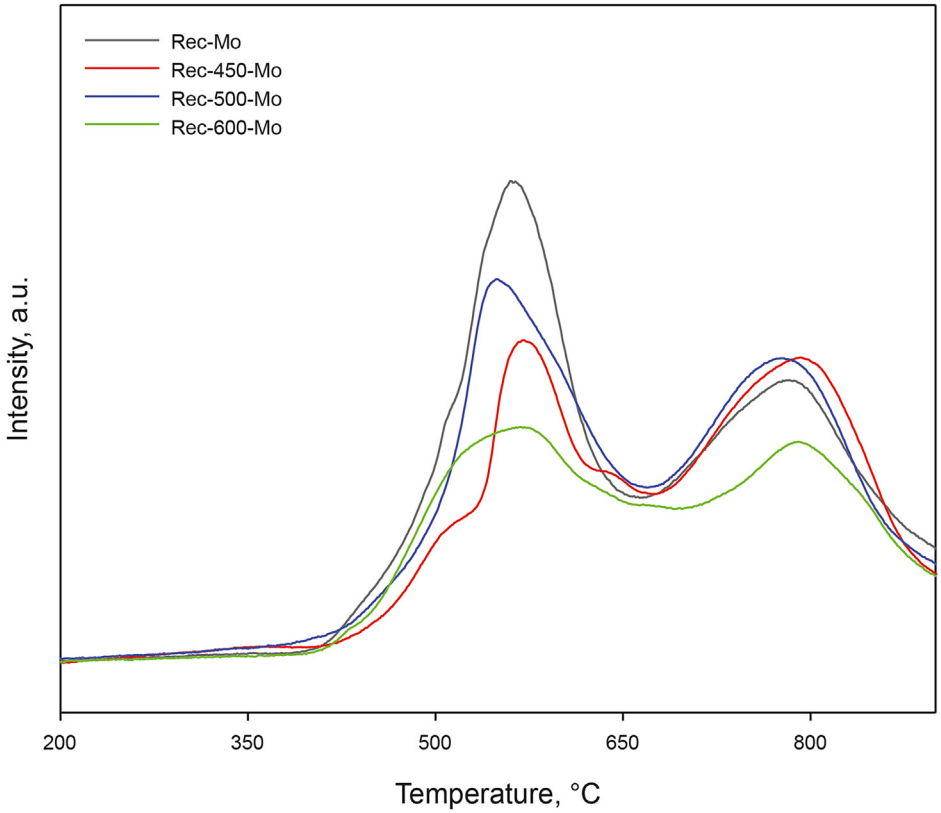

Fig. 5. H_2-TPR profiles of Mo catalysts supported on rectorites calcined at different temperatures.

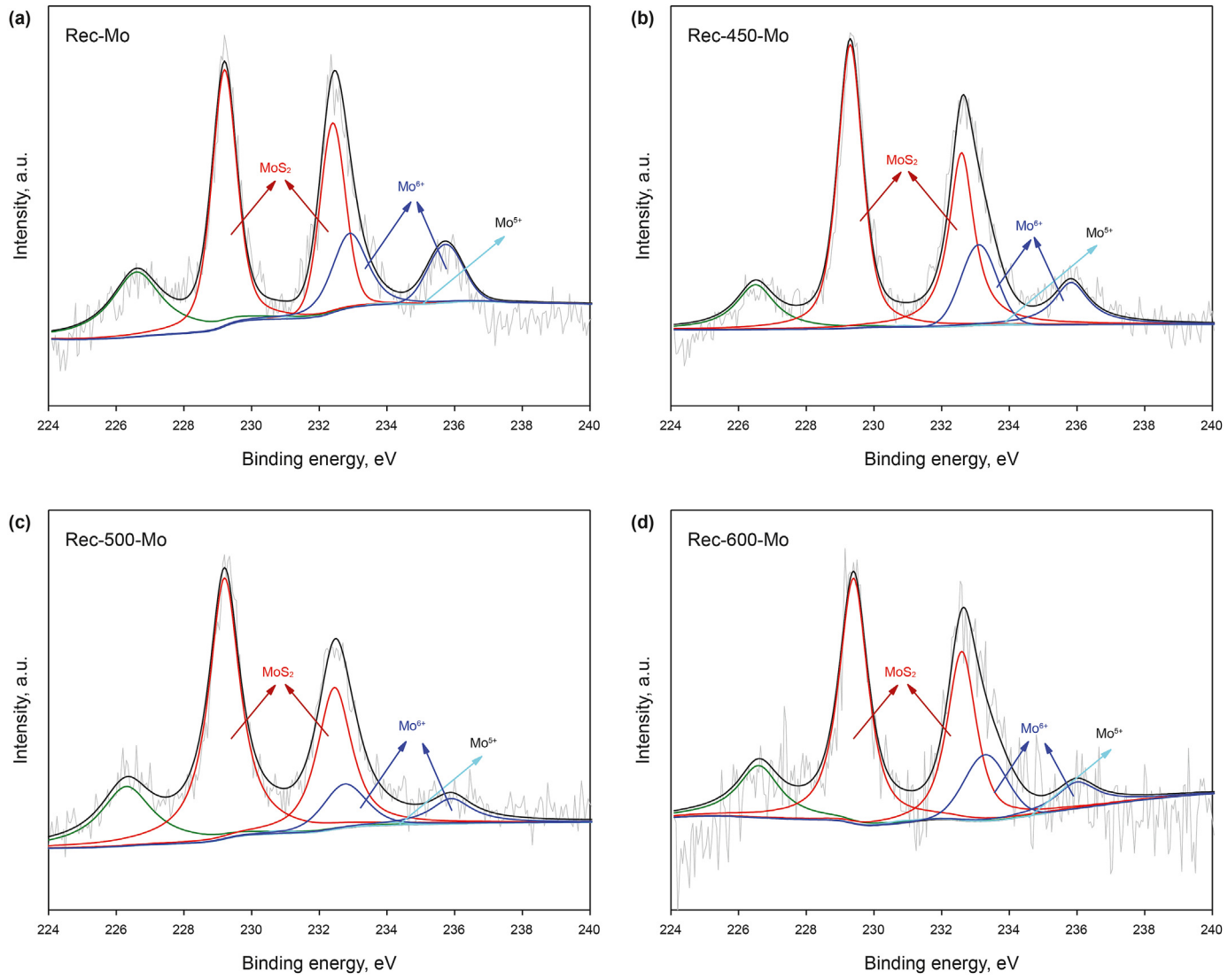

Fig. 6. Mo 3d XPS spectra and deconvolution results of sulfide catalysts supported on rectorites calcined at different temperatures.

Table 4
Mo(3d) XPS deconvolution results of sulfided catalysts.

Catalysts	Mo percentage, %			$Mo_{sulfidation}$, %
	Mo^{4+}	Mo^{5+}	Mo^{6+}	
Rec-Mo	71	3	26	71
Rec-450-Mo	75	2	23	75
Rec-500-Mo	82	1	17	82
Rec-600-Mo	78	2	20	78

3.3. Catalytic performance

The performance of catalyst supported on calcined rectorite was evaluated in the slurry-phase hydrocracking of VR at 420 °C under an initial H_2 pressure of 13.0 MPa. Fig. 7 shows VR conversions of the different catalysts. The VR conversion of Rec-Mo catalyst was about 77.0 wt%, and no notable change of the conversion was observed for the catalysts supported on calcined rectorites, exceptionally Rec-450-Mo catalyst with VR conversion of 81.0 wt%. It has been reported that the slurry-phase hydrocracking over oil dispersed catalyst or catalyst with few acid sites occurred above 420 °C was considered as a thermal cracking reaction path accompanied with hydrocracking reaction path (Kim et al., 2017; Matsumura et al., 2005; Nguyen et al., 2013). The thermal cracking reaction followed free radical mechanism, mainly depending on the reaction temperature, while hydrocracking reaction followed carbenium ion mechanism, which was principally affected by the acid sites of catalysts at the same reaction condition. There were few acid sites in rectorites examined by Py-FTIR, shown in Table 3. Hence, it is concluded that the almost same VR conversions for all catalysts were attributed to the slurry-phase hydrocracking controlled by the thermal cracking reaction following free radical mechanism.

The products distribution is significant for the conversion of heavy and poor feedstocks into light oil fractions in the refining industry, in which more amount of the valuable fractions of naphtha and middle distillates corresponding to the boiling point range of gasoil and diesel was expected to produce, but gas and coke as worthless product, especially coke causing negative effect on the catalyst and reactor, were as infamous fraction. The yields of naphtha and middle distillates are shown in Fig. 7, and the products distribution of the catalysts supported on rectorites calcined at various temperatures are shown in Fig. 8. The yields of naphtha and

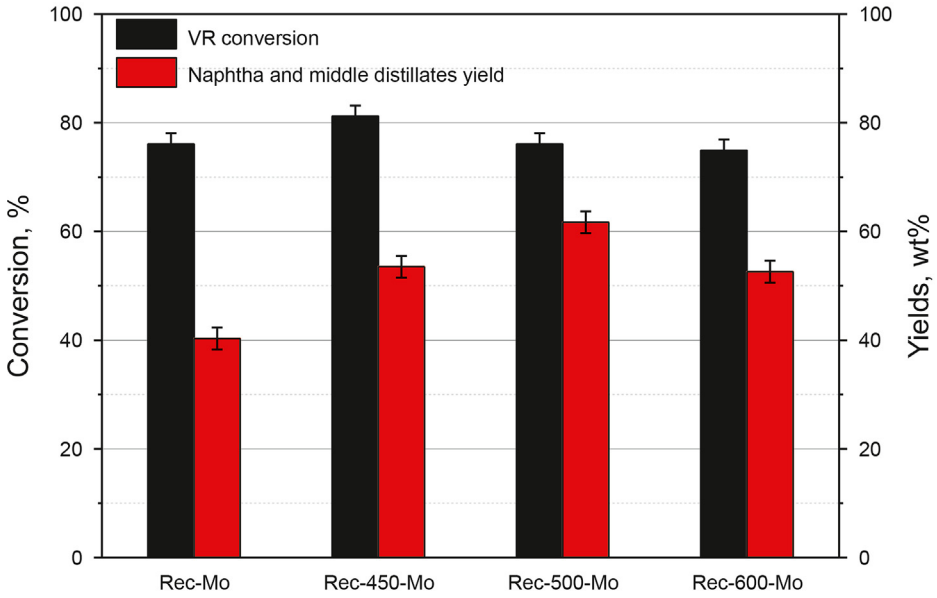

Fig. 7. VR conversions and yields of naphtha and middle distillates for the various catalysts.

middle distillates for the various catalysts increased following as Rec-Mo (40.4 wt%) < Rec-600-Mo (52.7 wt%) < Rec-450-Mo (53.5 wt%) < Rec-500-Mo (61.7 wt%), indicating that the calcination of rectorite was beneficial for the enhancement of the yields of naphtha and middle distillates in the slurry-phase hydrocracking process.

The detail yields of gas, naphtha, middle distillates, VGO, residues and coke of the various catalysts were distinctly different, as shown in Fig. 8. Rec-Mo catalyst presented the naphtha yield of 14.9 wt% and middle distillates yield of 25.5 wt%, both of which obviously increased for the catalysts supported on calcined rectorites, especially Rec-500-Mo catalyst with the naphtha yield of 25.4 wt% and middle distillates yield of 36.3 wt%. Moreover, the gas yield of Rec-Mo catalyst was up to 28.2 wt%, distinctly higher than that of the catalysts supported on calcined rectorites, and the gas yield of Rec-500-Mo catalyst reduced to 7.9 wt%. In addition, there was no remarkable change on the coke yield for the various catalysts. It is concluded that the catalysts supported on calcined rectorite had better performance compared with Rec-Mo catalyst on the basis of product distribution, especially Rec-500-Mo catalyst, it is attributed that the higher hydrogenation activity of the catalyst restrained over cracking reaction of intermediate product to produce gas.

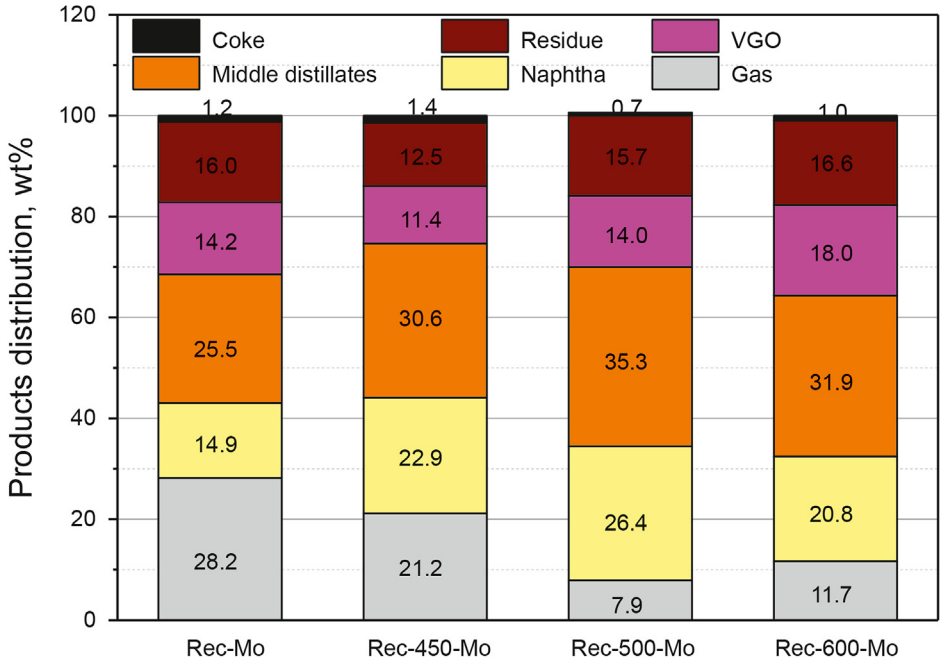

Fig. 8. Products distribution of VR hydrocracking for the various catalysts.

4. Conclusions

In this study, the catalysts supported on natural rectorite were prepared, and the effect of calcination modification on the catalysts properties was examined. The catalyst performance was conducted in an autoclave reactor at 420 °C and an initial H_2 pressure of 13 MPa. The reaction results show that the catalysts supported on calcined rectotire exhibited similar VR conversions with the catalyst supported on raw rectorite, it is ascribed that the thermal cracking reaction following free radical mechanism controlled the reaction process, because there were few acid sites on the catalyst surface. However, the yields of naphtha and middle distillates for the catalysts supported on calcined rectorite were obviously higher compared with that on raw rectorite, especially the yields of naphtha and middle distillates over Rec-500-Mo catalyst up to 61.7 wt%, indicating that the calcination of rectorite was beneficial for improving the yields of naphtha and middle distillates in the slurry-phase hydrocracking process, it is attributed that the higher sulfidation degree of molybdenum oxide species on catalyst promoted the hydrogenation reaction, thus inhibited the over-cracking reaction of intermediate product to produce gas. This study is significant for the development of high-efficient and low-cost catalyst for the slurry-phase hydrocracking of heavy and poor oil.

Acknowledgments

The authors acknowledge National Key Research and Development program (2018YFA0209403) and National Natural Science Foundation of China (Youth) program (21908027) for financing this research.

References

Al-Attas, T., Ali, S.A., Zahir, M.H., Xiong, Q., Hossain, M.M., 2019. Recent advances in heavy oil upgrading using dispersed catalysts. Energy Fuels 33, 7917–7949. https://doi.org/10.1021/acs.energyfuels.9b01532.

Bao, T., Damtie, M.M., Wu, k, Wei, X.L., Zhang, Y., Chen, J., Deng, C.X., Jin, J., Yu, Z.M., Wang, L., Frost, R.L., 2019. Rectorite-supported nano-Fe_3O_4 composite materials as catalyst for pchlorophenol degradation: preparation, characterization, and mechanism. Appl. Clay Sci. 176, 66–77. https://doi.org/10.1016/j.clay.2019.04.020.

Bellussi, G., Rispoli, G., Landoni, A., Millini, R., Pollesel, P., 2013. Hydroconversion of heavy residues in slurry reactors: developments and perspectives. J. Catal. 308, 189–200. https://doi.org/10.1016/j.jcat.2013.07.002.

Cheng, K., Virginie, M., Ordomsky, V.V., Cordier, C., Chernavskii, P.A., Ivantsov, M.I., Paul, S., Wang, Y., Khodakov, A.Y., 2015. Pore size effects in high-temperature Fischer–Tropsch synthesis over supported iron catalysts. J. Catal. 328, 139–150. https://doi.org/10.1016/j.jcat.2014.12.007.

Cortes, J.C., Scott, C.E., Pereira-Almao, P., Molina, R., Moreno, S., 2019. Modified vermiculite for hydrocracking of athabasca bitumen. Energy Fuels 33, 5153–5161. https://doi.org/10.1021/acs.energyfuels.9b00938.

Cui, Q.Y., Zhou, Y.S., Wei, Q., Yu, G.L., Zhu, L., 2013. Performance of Zr- and P-modified USY-based catalyst in hydrocracking of vacuum gas oil. Fuel Process. Technol. 106, 439–446. https://doi.org/10.1016/j.fuproc.2012.09.010.

Du, J.T., Deng, W.A., Li, C., Zhang, Z.L., Yang, T.F., Cao, X.P., 2018. Multi-metal catalysts for slurry-phase hydrocracking of coal-tar vacuum residue: impact of inherent inorganic minerals. Fuel 215, 370–377. https://doi.org/10.1016/j.fuel.2017.09.120.

Go, K.S., Lim, S.H., Kim, Y.K., Kwon, E.H., Nho, N.S., 2018. Characteristics of slurry-phase hydrocracking for vacuum residue with reaction temperature and concentrations of MoS_2 dispersed catalysts. Catal. Today 305, 92–101. https://doi.org/10.1016/j.cattod.2017.09.008.

Kang, K.H., Nguyen, N.T., Seo, H., Kim, G.T., Park, S., 2020. Slurry-phase hydrocracking of heavy oil over Mo precursors: effect of triphenylphosphine ligands. J. Catal. 384, 106–121. https://doi.org/10.1016/j.jcat.2020.02.007.

Kim, K., Lee, Y., 2019. Promotional effect of Co on unsupported MoS_2 catalysts for slurry phase hydrocracking of vacuum residue: X-ray absorption fine structure studies. J. Catal. 380, 278–288. https://doi.org/10.1016/j.jcat.2019.09.040.

Kim, S., Kim, K., Lee, Y., 2017. Effects of dispersed MoS_2 catalysts and reaction conditions on slurry phase hydrocracking of vacuum residue. J. Catal. 347, 27–137. https://doi.org/10.1016/j.jcat.2016.11.015.

Kim, S., Kim, K., Lee, D., Lee, Y., 2018. Structure and activity of dispersed Co, Ni, or Mo sulfides for slurry phase hydrocracking of vacuum residue. J. Catal. 364, 131–140. https://doi.org/10.1016/j.jcat.2018.05.002.

Li, C., Du, J.T., Yang, T., Deng, W., 2019. Exploratory investigation on the slurry-phase hydrocracking reaction behavior of coal tar and petroleum-based heavy oil mixed raw material. Energy Fuels 33, 8471–8482. https://doi.org/10.1021/acs.energyfuels. 9b02031.

Lim, S.H., Go, K.S., Nho, N.S., Lee, J.G., 2018. Effect of reaction temperature and time on the products and asphaltene dispersion stability in slurry-phase hydrocracking of vacuum residue. Fuel 234, 305–311. https://doi.org/10.1016/j.fuel.2018.06.113.

Liu, B., Zhao, K.D., Chai, Y.M., Li, Y.P., Liu, D., Liu, Y.Q., Liu, C.G., 2019. Slurry phase hydrocracking of vacuum residue in the presence of presulfided oil-soluble MoS_2 catalyst. Fuel 246, 133–140. https://doi.org/10.1016/j.fuel.2019.02.114.

Liu, H.Y., Yue, Y.Y., Shen, T., Wang, W.W., Li, T.S., Bao, X.J., 2019. Transformation and crystallization behaviors of titanium species in synthesizing Ti-ZSM-5 zeolites from natural rectorite mineral. Ind. Eng. Chem. Res. 58, 11861–11870. https://doi.org/10.1021/acs.iecr.9b01826.

Liu, X.D., Wei, Q., Huang, W.B., Zhou, Y.S., Zhang, P.F., Xu, Z.S., 2020. DFT insights into the stacking effects on HDS of 4,6-DMDBT on Ni-Mo-S corner sites. Fuel 280, 118669–118674. https://doi.org/10.1016/j.fuel.2020.118669.

Looi, P.Y., Mohamed, A.R., Tye, C.T., 2012. Hydrocracking of residual oil using molybdenum supported over mesoporous alumina as a catalyst. Chem. Eng. J. 181–182, 717–724. https://doi.org/10.1016/j.cej.2011.12.080.

Matsumura, A., Kondo, T., Sato, S., Saito, I., De Souza, W.F., 2005a. Hydrocracking brazilian marlim vacuum residue with natural limonite. Part 1: catalytic activity of natural limonite. Fuel 84, 411–416. https://doi.org/10.1016/j.fuel.2004.09.014.

Matsumura, A., Sato, S., Kondo, T., Saito, I., De Souza, W.F., 2005b. Hydrocracking marlim vacuum residue with natural limonite. Part 2: experimental cracking in a slurry-type continuous reactor. Fuel 84, 417–421. https://doi.org/10.1016/j.fuel.2004.09.015.

Mogorosi, R.P., Fischer, N., Claeys, M., Steen, E.V., 2012. Strong-metal–support interaction by molecular design: Fe–silicate interactions in Fischer–Tropsch catalysts. J. Catal. 289, 140–150. https://doi.org/10.1016/j.jcat.2012.02.002.

Nguyen, M.T., Nguyen, N.T., Cho, J., Park, C., Park, S., Jung, J., Lee, C.W., 2016. A review on the oil-soluble dispersed catalyst for slurry-phase hydrocracking of heavy oil. J. Ind. Eng. Chem. 43, 1–12. https://doi.org/10.1016/j.jiec.2016.07.057.

Nguyen, T.S., Tayakout-Fayolle, M., Lacroix, M., Gotteland, D., Aouine, M., Bacaud, R., Afanasiev, P., Geantet, C., 2015. Promotion effects with dispersed catalysts for residue slurry hydroconversion. Fuel 160, 50–56. https://doi.org/10.1016/j.fuel.2015.07.012.

Nguyen, T.S., Tayakout-Fayolle, M., Ropars, M., Geantet, C., 2013. Hydroconversion of an atmospheric residue with a dispersed catalyst in a batch reactor: kinetic modeling including vapor–liquid equilibrium. Chem. Eng. Sci. 94, 214–223. https://doi.org/10.1016/j.ces.2013.02.036.

Nguyen-Huy, C., Kweon, H., Kim, H., Kim, D.K., Kim, D., Oh, S.H., Shin, E.W., 2012. Slurry-phase hydrocracking of vacuum residue with a disposable red mud catalyst. Appl Catal A 447– 448, 186–192. https://doi.org/10.1016/j.apcata.2012.09.043.

Nguyen-Huy, C., Pham, V.H., Kim, D.K., Kim, D., Oh, S.H., Chung, J.S., Kim, W., Shin, E.W., 2013. Role of macroporosity in macro-mesoporous red mud catalysts for slurry-phase hydrocracking of vacuum residue. Appl Catal A 468, 305–312. https://doi.org/10.1016/j.apcata.2013.08.031.

Nikulshin, P.A., Ishutenko, D.I., Mozhaev, A.A., Maslakov, K.I., Pimerzin, A.A., 2014. Effects of composition and morphology of active phase of $CoMo/Al_2O_3$ catalysts prepared using Co_2Mo_{10}–heteropolyacid and chelating agents on their catalytic properties in HDS and HYD reactions. J. Catal. 312, 152–169. https://doi.org/10.1016/j.jcat.2014.01.014.

Park, H., Lee, Y., 2019. Designing supported $NiMoS_2$ catalysts for hydrocracking of vacuum residue. Fuel 239, 1265–1273. https://doi.org/10.1016/j.fuel.2018.10.154.

Pimerzin, A., Mozhaev, A., Varakin, A., Maslakov, K., Nikulshin, P., 2017. Comparison of citric acid and glycol effects on the state of active phase species and catalytic properties of $CoPMo/Al_2O_3$ hydrotreating catalysts. Appl. Catal., B 205, 93–103. https://doi.org/10.1016/j.apcatb.2016.12.022.

Puron, H., Pinilla, J.L., Berrueco, C., Fuente, J.A.M.D.L., Millan, M., 2013. Hydrocracking of maya vacuum residue with NiMo catalysts supported on mesoporous alumina and silica–alumina. Energy Fuels 27, 3952–3960. https://doi.org/10.1021/ef400623f.

Quitian, A., Ancheyta, J., 2016. Partial upgrading of heavy crude oil by slurry-phase hydrocracking with analytical grade and ore catalysts. Energy Fuels 30, 10117–10125. https://doi.org/10.1021/acs.energyfuels.6b01648.

Sahu, R., Song, B., Jeon, Y.P., Lee, C.W., 2016. Upgrading of vacuum residue in batch type reactor using Ni–Mo supported on goethite catalyst. J. Ind. Eng. Chem. 35, 115–122. https://doi.org/10.1016/j.jiec.2015.12.017.

Sanaie, N., Watkinson, A.P., Bowen, B.D., Smith, K.J., 2001. Effect of minerals on coke precursor formation. Fuel 80, 1111–1119. https://doi.org/10.1016/S0016-2361(00)00176-9.

Sanchez, J., Moreno, A., Mondragon, F., Smith, K.J., 2018. Morphological and structural properties of MoS_2 and MoS_2-amorphous silica-alumina dispersed catalysts for slurry-hase hydroconversion. Energy Fuels 32, 7066–7077. https://doi.org/10.1021/acs.energyfuels.8b01081.

Tan, Q.F., Fan, Y., Liu, H.Y., Song, T.C., Shi, G., Shen, B.J., Bao, X.J., 2008. Bimodal micro-mesoporous aluminosilicates for heavy oil cracking: porosity tuning and catalytic properties. AIChE J. 54, 1850–1859. https://doi.org/10.1002/aic.11512.

Viet, T.T., Lee, J., Ryu, J.W., Ahn, I.S., Lee, C., 2012. Hydrocracking of vacuum residue with activated carbon in supercritical hydrocarbon solvents. Fuel 94, 556–562. https://doi.org/10.1016/j.fuel.2011.09.007.

Watanabe, I., Otake, M., Yoshimoto, M., Sakanishi, K., Korai, Y., Mochida, I., 2002.

Behaviors of oil-soluble molybdenum complexes to form very fine MoS_2 particles in vacuum residue. Fuel 81, 1515–1520. https://doi.org/10.1016/S0016-2361(02)00070-4.

Wei, Q., Zhang, J.R., Liu, X.D., Zhang, P.F., Wang, S.Q., Wang, Y., Zhang, Z.L., Zhang, T., Zhou, Y.S., 2019. Citric acid-treated zeolite Y(CY)/zeolite Beta composites as supports for vacuum gas oil hydrocracking catalysts: high yield production of highly-aromatic heavy naphtha and low-BMCI value tail oil. Frontiers in Chemistry 7, 705–715. https://doi.org/10.3389/fchem.2019.00705.

Yang, T., Liu, C., Deng, W., Li, C., Niu, Q., 2019. Influence of the iron proportion on the efficiency of an oil-soluble Ni–Fe catalyst applied in the Co-liquefaction of lignite and heavy residue. Ind. Eng. Chem. Res. 58, 19072–19081. https://doi.org/10.1021/acs.iecr.9b04529.

Yue, Y.Y., Niu, P.L., Jiang, L.L., Cao, Y.N., Bao, X.J., 2016. Acid-Modified natural bauxite mineral as a cost-effective and high efficient catalyst support for slurry-phase hydrocracking of high temperature coal tar. Energy Fuels 30, 9203–9209. https://doi.org/10.1021/acs.energyfuels.6b01869.

Yue, Y.Y., Li, J.W., Dong, P., Wang, T.H., Jiang, L.L., Yuan, P., Zhu, H.B., Bai, Z.S., Bao, X.J., 2018. From cheap natural bauxite to high-efficient slurry-phase hydrocracking catalyst for high temperature coal tar: a simple hydrothermal modification. Fuel Process. Technol. 175, 123–130. https://doi.org/10.1016/j.fuproc.2018.03.006.

Zhang, G.K., Guo, Y.D., Gao, Y.Y., Zhang, Y.L., 2010. Fe_2O_3-pillared rectorite as an efficient and stable fenton-like heterogeneous catalyst for photodegradation of organic contaminants. Environ. Sci. Technol. 44, 6384–6389. https://doi.org/10.1021/es1011093.

Zheng, P.W., Chang, P.R., Ma, X.F., 2013. Preparation and characterization of rectorite gels. Ind. Eng. Chem. Res. 52, 5066–5071. https://doi.org/10.1021/ie3027372.

Zhou, W.W., Wei, Q., Zhou, Y.S., Liu, M.F., Ding, S.J., Yang, Q., 2018. Hydrodesulfurization of 4,6-dimethyldibenzothiophene over NiMo sulfide catalysts supported on meso-microporous Y zeolite with different mesopore sizes. Appl. Catal., B 238, 212–224. https://doi.org/10.1016/j.apcatb.2018.07.042.